Supplemental Materials for

Source-dependent organic aerosol hygroscopicity in eastern China: observational evidence for conditional enhancement under biomass-burning influence

Yunfei Wu[1*], Jiwei Li[2], Zhisheng Zhang[3], Jun Tao[4], Yunjie Xia[5], Liang Ran[1], Zhaoze Deng[1*]

[1]State Key Laboratory of Atmospheric Environment and Extreme Meteorology, Institute of Atmospheric Physics, Chinese Academy of Sciences, Beijing 100029, China

[2]School of Resources and Environmental Engineering, Shandong University of Technology, Zibo 255000, China

[3]South China Institute of Environmental Sciences, Ministry of Ecology and Environmental, Guangzhou 510655, China

[4]Institute for Environmental and Climate Research, College of Environment and Climate, Jinan University, Guangzhou 511436, China

[5]Beijing Meteorological Observation Center, Beijing 100176, China

Correspondence to: Yunfei Wu (wuyf@mail.iap.ac.cn) and Zhaoze Deng (dengzz@mail.iap.ac.cn)

Text S1: Source apportionment of organic aerosol

The identified factors in winter included hydrocarbon-like OA (HOA), associated with traffic emissions; cooking-related OA (COA); biomass burning OA (BBOA); and oxygenated OA (OOA), representing secondary oxidized components. In contrast, summer OA mass spectra were adequately described by two factors, denoted as HOA and OOA. The spectrum of each OA factor is shown in Figure S1.

In the mass spectrum of HOA, hydrocarbon ions (i.e., $C_nH_{2n-1}^+$ and $C_nH_{2n+1}^+$) exhibit distinct peaks, such as those at m/z 41, 43, 55, 57, 69, 71, 83 and 85. HOA is associated with the combustion of fossil fuels, including gasoline/diesel exhaust and engine lubricating oil, and is mainly composed of nalkanes, branched alkanes, cycloalkanes and aromatic hydrocarbons. HOA correlates well with BC (R = 0.75 in winter and R = 0.95 in summer). The elevated HOA fraction in the morning is attributable to traffic emissions, as supported by concurrent peaks in NO and CO concentrations (Figure S9). COA is primarily composed of fatty acids derived from edible oils, along with glycerides and saccharides. The mass spectrum of COA resembles that of HOA, yet COA shows significantly higher signals at m/z 41 ($C_3H_5^+$) and 55 ($C_4H_7^+$). Accordingly, the ratios of m/z 41/43 and m/z 55/57 are generally utilized for the identification of COA. In the present analysis, the m/z 41/43 and m/z 55/57 ratios of COA were measured to be 1.3 and 2.1, respectively, which were notably higher than the corresponding values of HOA (0.8 and 1.1). A significant correlation is observed between m/z 98 and COA (R = 0.87 in winter). BBOA displays peaks at m/z 60 and 73 in its mass spectrum. These two fragments are derived from levoglucosan (m/z 60, $C_2H_4O_2^+$) and mannosan (m/z 73, $C_3H_5O_2^+$), generated during the pyrolysis and incomplete combustion of cellulose and hemicellulose, respectively. BBOA exhibits a significant correlation with m/z 60 (R = 0.89 in winter). In the evening, residential biomass burning and cooking activities likely contribute to the simultaneous increases in BBOA and COA mass fractions. OOA denotes oxidized organic aerosol. Oxidized ionic fragments present peaks, with a prominent signal at m/z 44 (mainly CO_2^+) and a minor contribution from m/z 43 ($C_2H_3O^+$). OOA is higher in the afternoon and lower during the morning and evening hours, which is significantly correlated with m/z 44 variations in winter (R = 1.00) and in summer (R = 1.00).

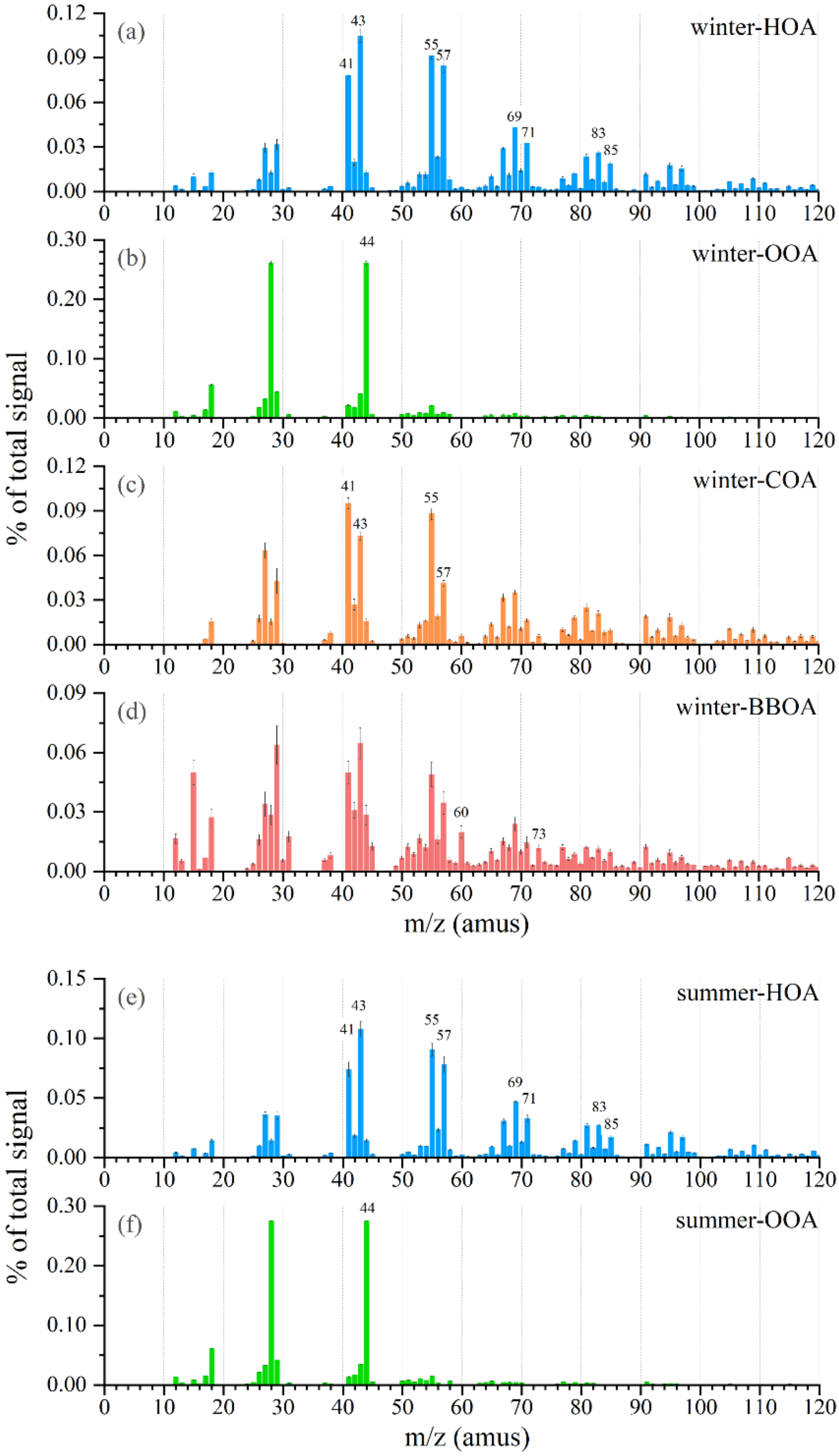

Figure S1: The spectrum of OA factor in winter (a-d) and summer (e-f) resolved by the PMF model.

Text S2: Interaction analysis of biomass-burning contribution and oxidation state on OA hygroscopicity

To further quantify the coupled influences of biomass-burning contribution and oxidation state on OA hygroscopicity, an interaction regression model was established using the biomass-burning fraction (f_{bb}), the O:C ratio, and their interaction term:

$$\kappa_{OA} = a_0 + a_1 \times f_{bb} + a_2 \times (O{:}C) + a_3 \times (f_{bb} \cdot (O{:}C)).$$

The fitted coefficients were a_0 = 0.895, a_1 = -0.024, a_2 = -1.229, and a_3 = 0.038. All coefficients were statistically significant ($p < 0.001$), indicating that both biomass-burning contribution and oxidation state, as well as their interaction, exert significant influences on OA hygroscopicity. The positive interaction coefficient ($a_3 > 0$) demonstrates that the effect of oxidation on κ_{OA} is not constant but depends on the contribution of biomass-burning aerosol.

The interaction model reproduced the observed variability in κ_{OA} reasonably well, yielding a correlation coefficient of 0.51 ($p < 0.001$) between fitted and observed κ_{OA}. Although this represents only a modest improvement over the simple correlation between κ_{OA} and f_{bb} (R = 0.48), the principal purpose of the interaction model is not to maximize predictive skill, but rather to evaluate whether oxidation exerts different influences under different source conditions.

The dependence of κ_{OA} on oxidation state can be expressed by the partial derivative of the interaction model with respect to the O:C ratio,

$$\partial \kappa_{OA} / \partial\, (O{:}C) = a_2 + a_3 \times f_{bb} = -1.229 + 0.038 \times f_{bb},$$

This expression indicates that the sensitivity of κ_{OA} to oxidation increases systematically with increasing biomass-burning contribution. Under conditions of weak biomass-burning influence, the partial derivative remains negative or close to zero, suggesting that oxidation alone contributes little to enhancing OA hygroscopicity. As biomass-burning contribution increases, however, the oxidation dependence becomes progressively stronger, indicating that atmospheric aging substantially enhances the hygroscopicity of biomass-burning-derived OA.

Overall, the interaction analysis quantitatively supports the conclusion drawn from the observational analysis presented in the main text: aged biomass-burning contribution not only increases OA hygroscopicity directly but also modulates the extent to which atmospheric oxidation enhances hygroscopicity. These results suggest that source-dependent composition and oxidation state should be considered jointly when parameterizing OA hygroscopicity.

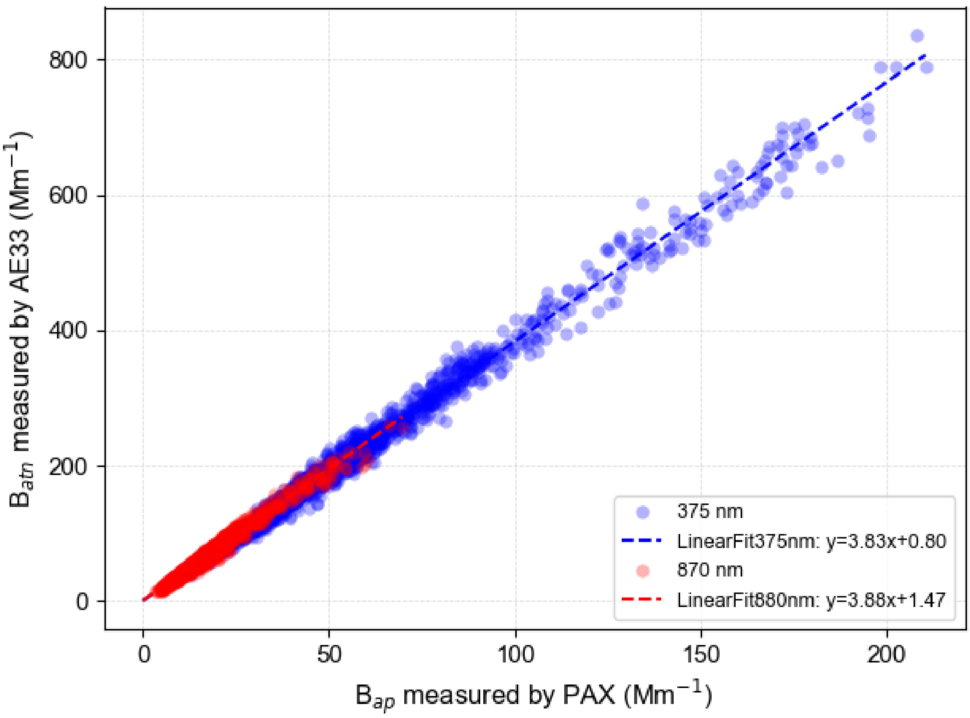

Figure S2: Intercomparison between attenuation coefficients (B_{atn}) measured by the AE33 aethalometer and aerosol absorption coefficients (B_{ap}) measured by photoacoustic extinctiometers (PAX). Different colors indicate measurements at two PAX operating wavelengths, with blue representing 375 nm and red representing 870 nm. Data points represent 30 min averaged values, and solid lines denote linear regressions of B_{atn} against B_{ap}. Since B_{atn} is directly measured by the AE33 at 370 and 880 nm, values at 375 and 870 nm were interpolated from adjacent wavelengths assuming a linear relationship between B_{atn} and wavelength in logarithmic space. The similar slopes of the regression lines at 375 and 870 nm suggest that the scattering effect on AE33 absorption measurements is largely wavelength-independent. Accordingly, a constant correction factor of 3.9 is applied to convert B_{atn} to B_{ap} across the seven AE33 operating wavelengths (370, 470, 520, 590, 660, 880, and 950 nm).

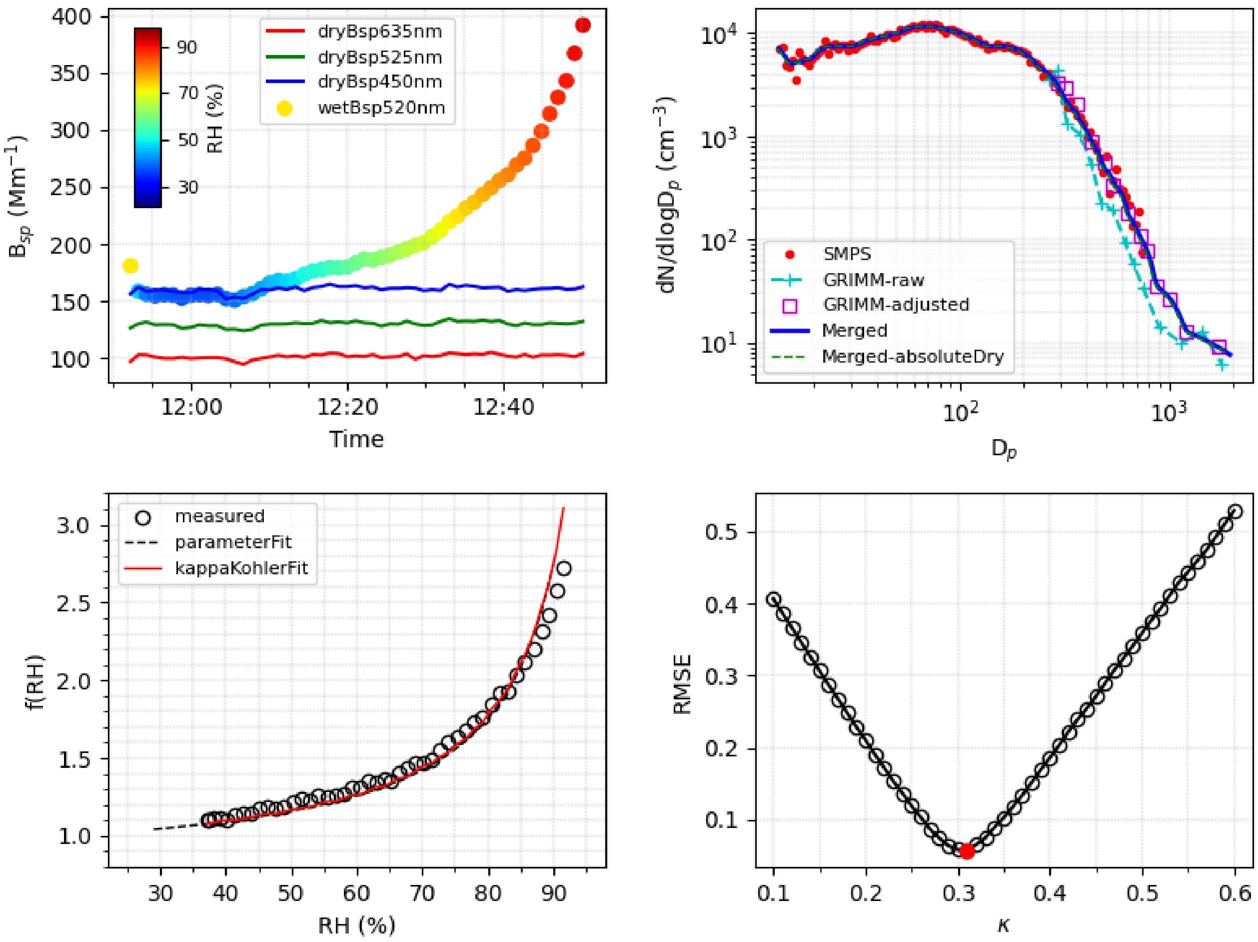

Figure S3: An example case of *f*(RH) measurements on January 16, 2021 (11:50–12:50) and κ inversion. The left-up panel shows the temporal variations of $B_{sp,dry}$ at 450 (blue line), 525 (green line) and 635 (red line) nm and $B_{sp,wet}$ colored by RH; the right-up panel shows the SMPS measured PNSD (red dots), raw Grimm derived PNSD (cyan dashed line), adjusted Grimm-derived PNSD (magenta squares), merged dry PNSD (blue solid line) and merged PNSD for absolutely dry aerosols (RH=0; green dashed line); the left-bottom panel shows measured *f*(RH) as a function of RH (black circles), parameter fitting for measured *f*(RH) (black dashed line) and optimal theoretical *f*(RH) (red solid line); the right-bottom panel shows the RMSE between measured *f*(RH) and theoretical *f*(RH) under different κ conditions, with the red dot representing the location of lowest RMSE.

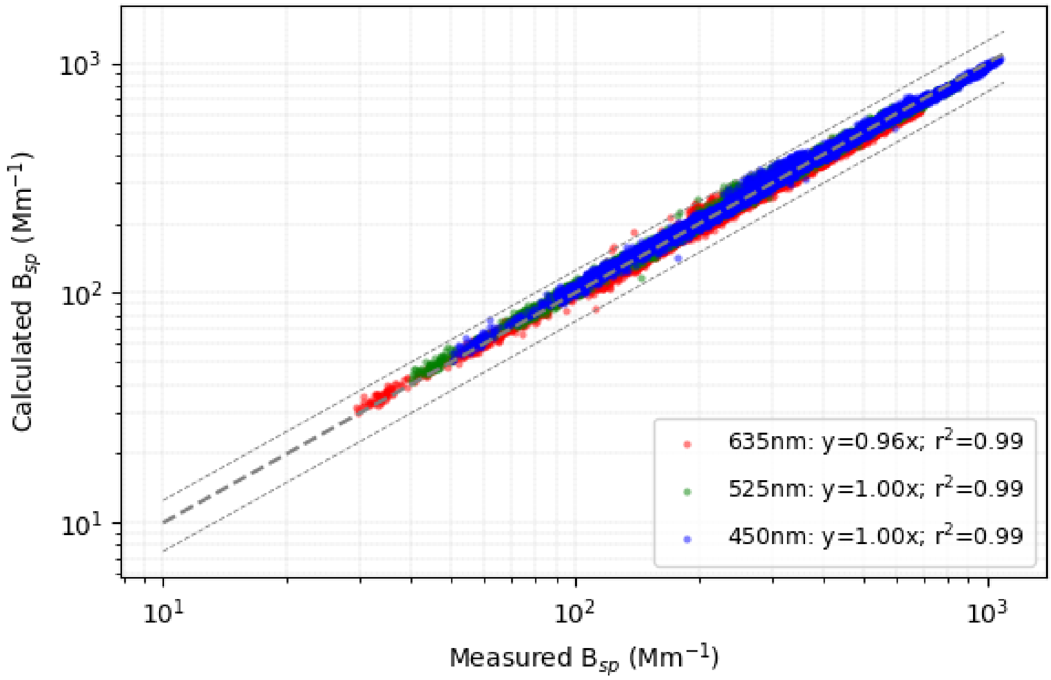

Figure S4: Comparation of B_{sp} calculated from the merged PNSD and optimal RI with the measured B_{sp} of dry aerosols at 450 (blue), 525 (green) and 635 (red) nm wavelengths during the winter campaign at Huainan. The thick dashed line represents the 1:1 line and the thin dashed lines represent ±25% bias.

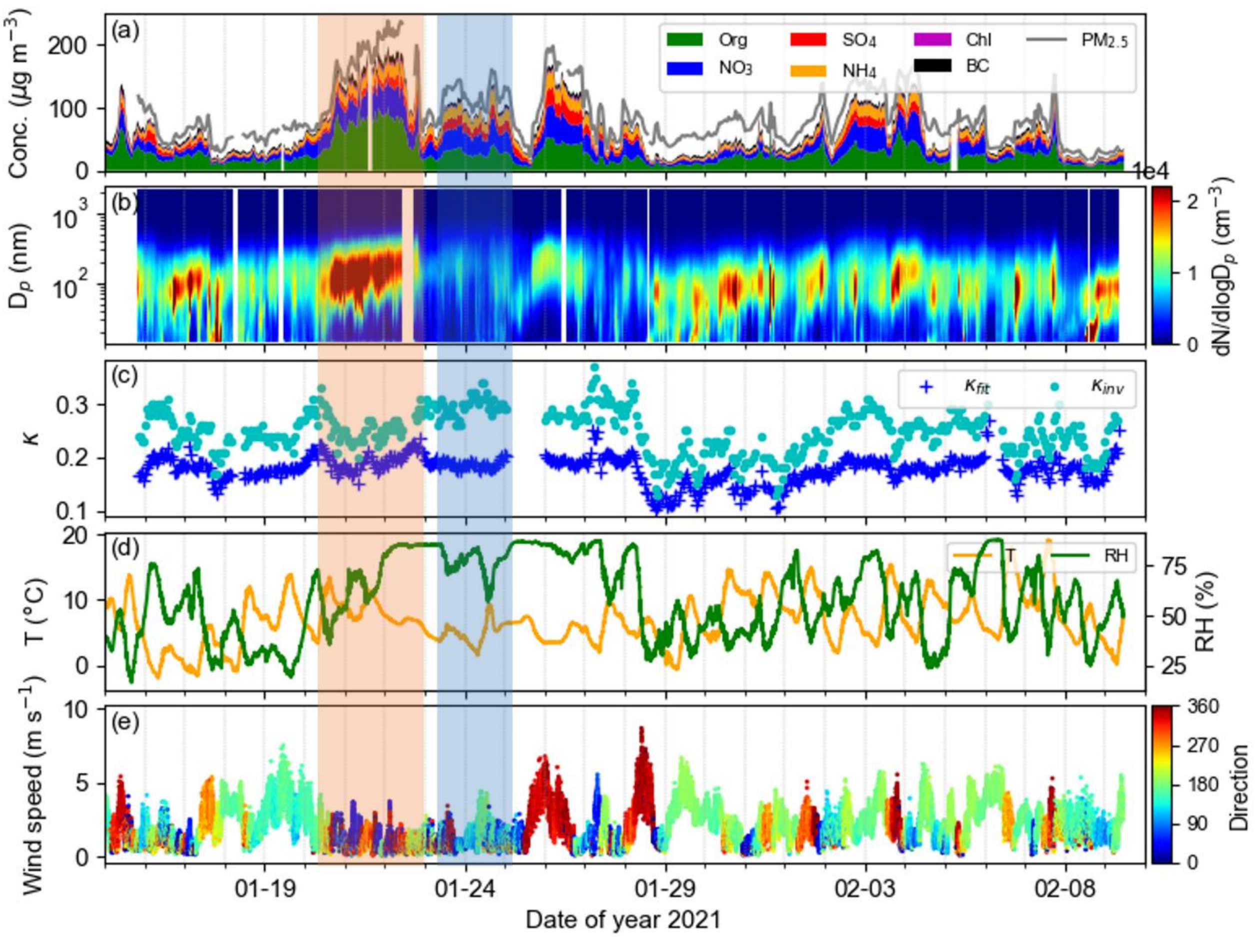

Figure S5: Time series of (a) $nrPM_{2.5}$ chemical composition mass concentrations, (b) particle number size distribution, (c) fitted and inverted hygroscopicity parameters (κ_{fit} and κ_{inv}), (d) air temperature (T) and relative humidity (RH), and (e) wind speed and direction at the Huainan site during the winter campaign. The shaded area denotes a persistent pollution episode from 20 to 25 January 2021, with different colors indicating distinct stages of the episode.

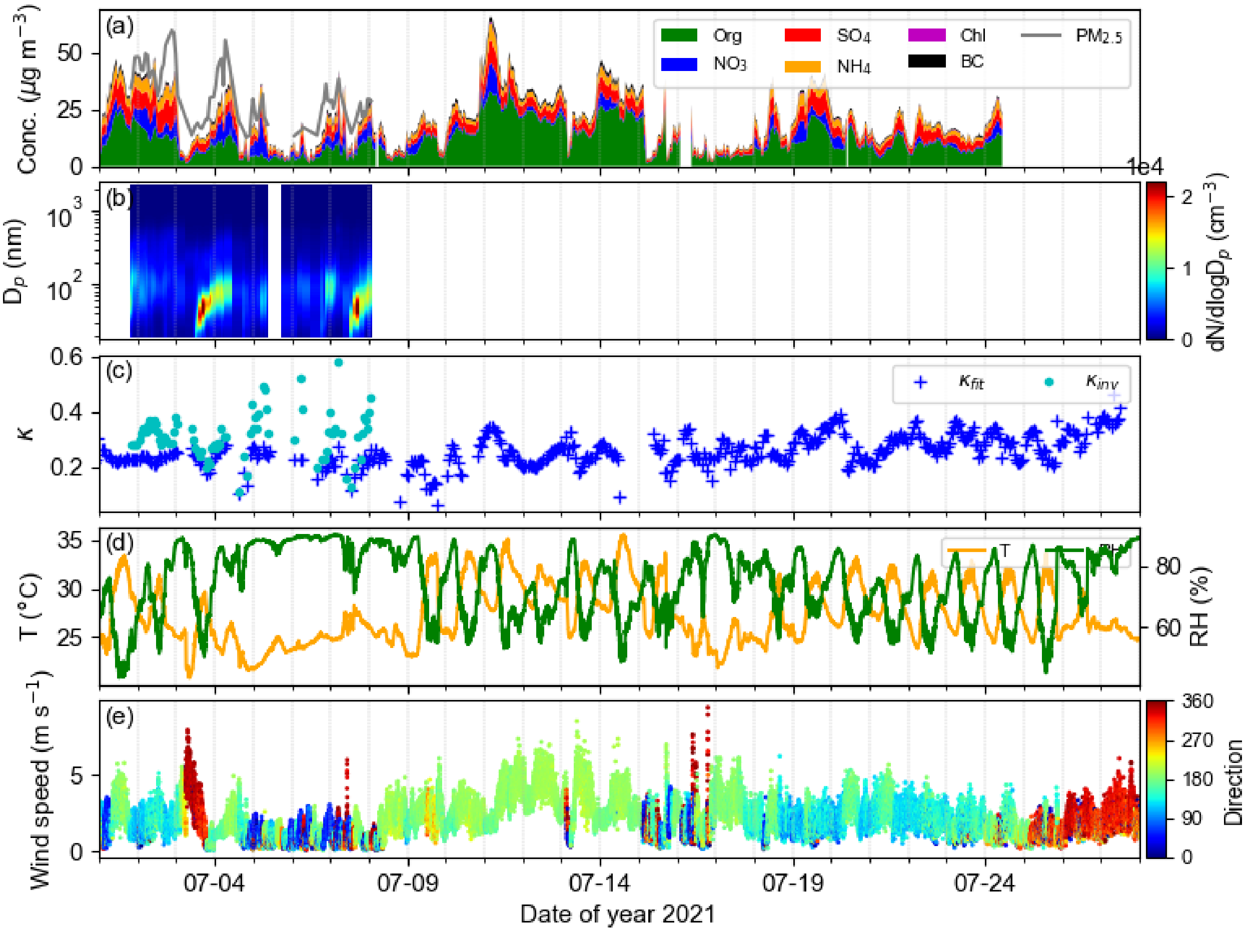

Figure S6: The same of Figure S5 but for the summer campaign. κ_{inv} was available for only six operational days (2 to 7 July 2021) due to CPC instrument failure.

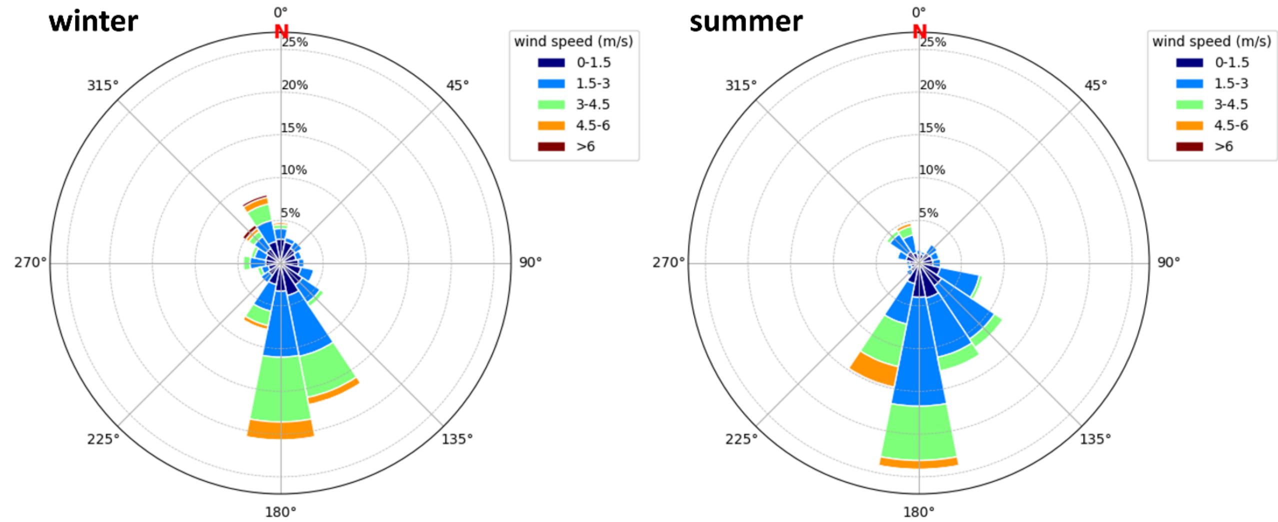

Figure S7: Wind roses plotted using minutely mean wind velocities and directions observed during winter and summer campaigns

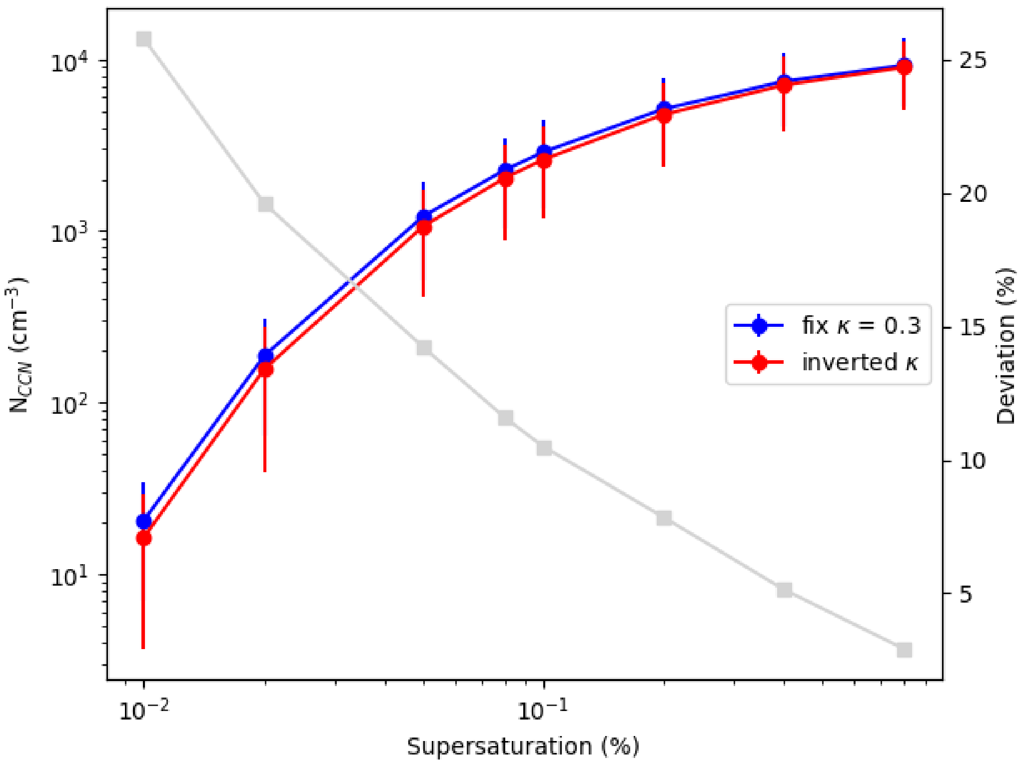

Figure S8: The average cloud condensation nuclei number concentration (N_{CCN}) estimated from the measured particle number size distribution (PNSD) during the winter campaign at Huainan, using a fixed hygroscopicity parameter (κ) of 0.3, as commonly assumed for continental aerosols (blue), and using measured κ values (red). The relative bias in N_{CCN} arising from assuming $\kappa = 0.3$, compared to calculations based on measured κ, is shown by the gray squares.

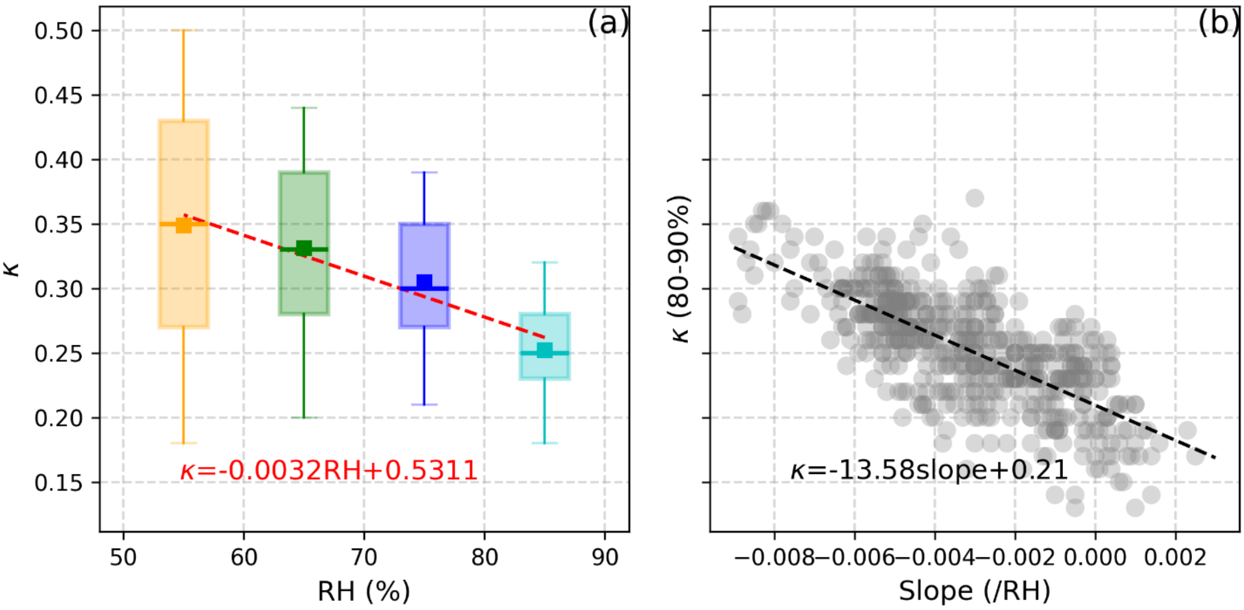

Figure S9: (a) Variation of κ_{inv} as a function of RH; (b) κ_{inv} values derived over the 80-90% RH range as a function of the linear regression slope of κ_{inv} versus RH. In panel (a), the upper and lower whiskers represent the 95th and 5th percentiles, respectively. The upper and lower edges of each box denote the 75th and 25th percentiles, while the median is indicated by a horizontal line within the box. Mean values are shown as solid square markers. The dashed line in panel (a) represents a linear regression of mean κ_{inv} versus RH, while in panel (b) the dashed line indicates the corresponding linear regression.

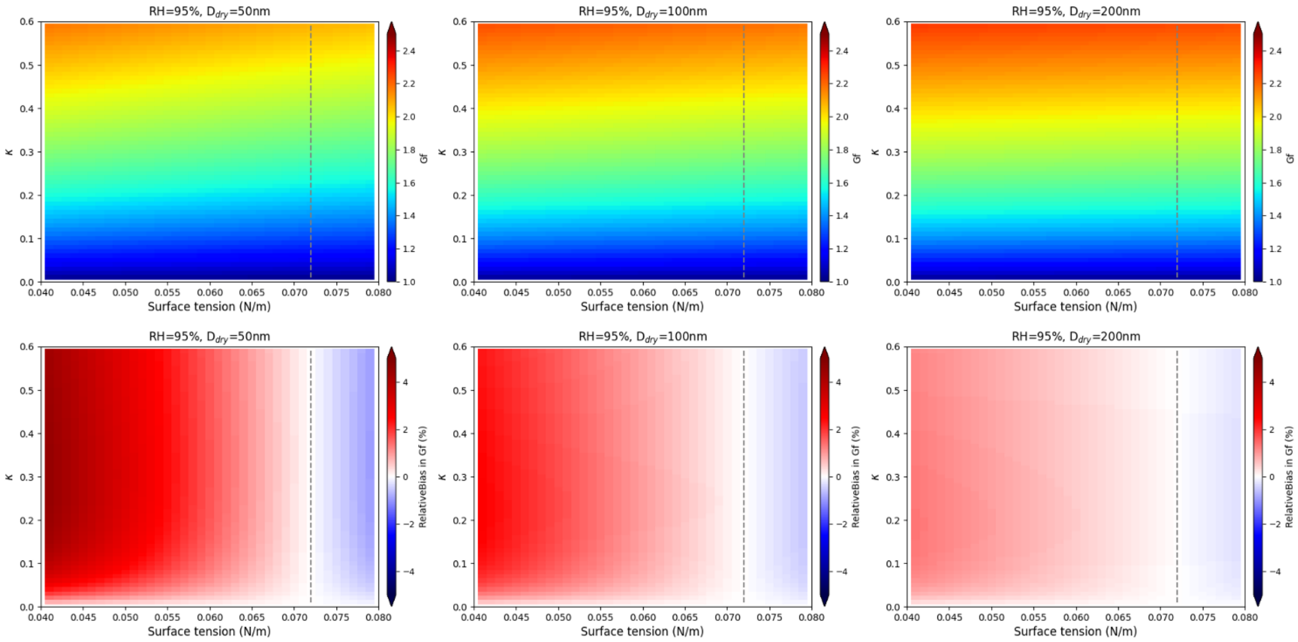

Figure S10: The κ-Köhler-derived g(RH=95%) (upper panels) and its relative deviation from values calculated using the surface tension of pure water ($\sigma_{s/a} \approx 0.072$ J m^{-2} at 25 °C and 1 atm) (lower panels), shown as functions of κ and $\sigma_{s/a}$ for typical-sized atmospheric particles (50, 100 and 200 nm). The largest relative deviations are 4.6%, 2.5% and 1.3% for particle diameters of 50, 100 and 200 nm, respectively, indicating $\sigma_{s/a}$ plays a negligible effect on aerosol hygroscopic growth under sub-saturation conditions.

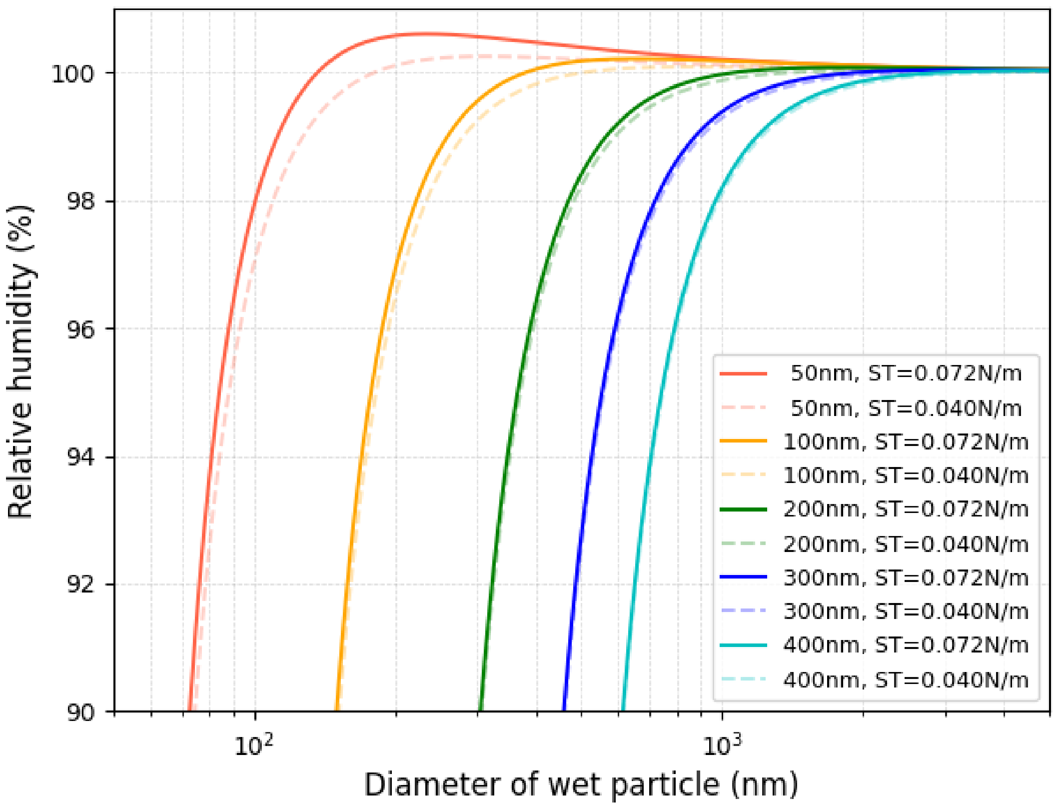

Figure S11: Köhler curves calculated using the κ-Köhler equation for five dry particle diameters (50, 100, 200, 300 and 400 nm). Solid lines represent calculations assuming the surface tension of pure water ($\sigma_{s/a}$ = 0.072 J m^{-2}), while dashed lines correspond to a plausibly lower-bound value of $\sigma_{s/a}$ = 0.04 J m^{-2}. The comparison illustrates that Köhler curves are relatively insensitive to surface tension under subsaturated conditions but become more sensitive under supersaturated conditions.

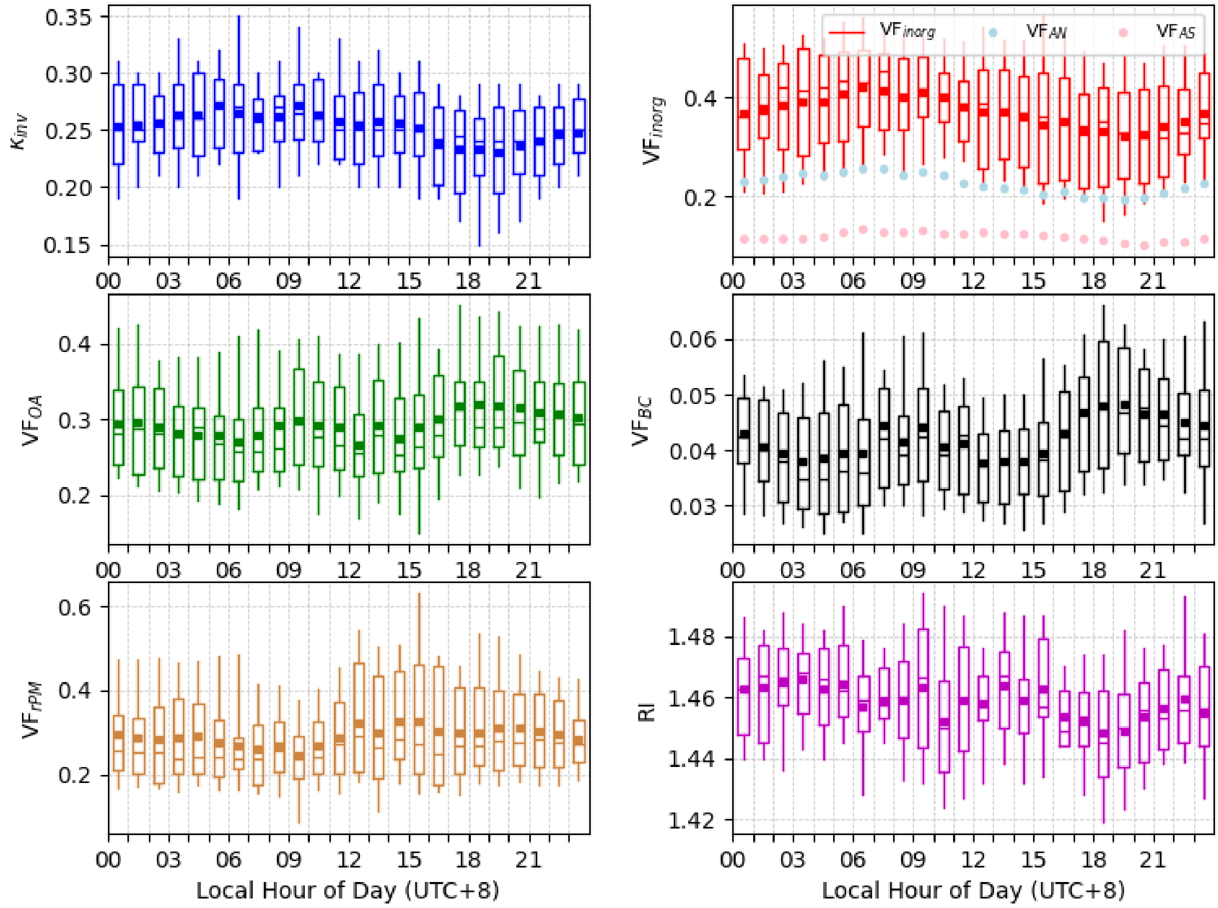

Figure S12: Diurnal variations of κ_{inv}, volume fraction of inorganic salts, OA, BC, rPM, and retrieved bulk refractive index during the winter campaign. The upper and lower bounds of each box represent the 75th and 25th percentiles, and the upper and lower whiskers represent the 95th and 5th percentiles. The line in each box is the median value and the square represents the mean.

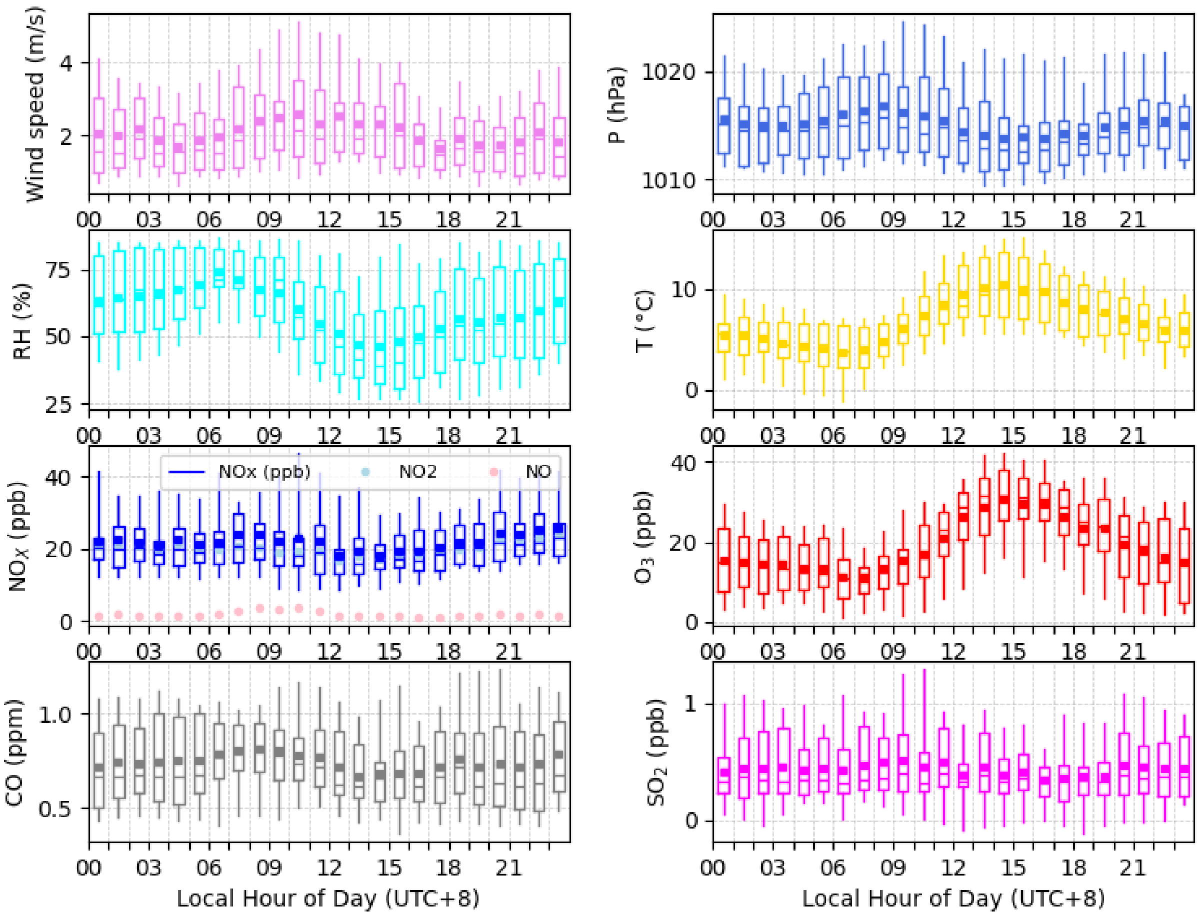

Figure S13: Diurnal variations of meteorological parameters including wind speed, pressure, relative humidity and air temperature, and mixing ratios of pollutant gases including NO_x, O_3, CO and SO_2 during the winter campaign. The upper and lower bounds of each box represent the 75^{th} and 25^{th} percentiles, and the upper and lower whiskers represent the 95^{th} and 5^{th} percentiles. The line in each box is the median value and the square represents the mean.

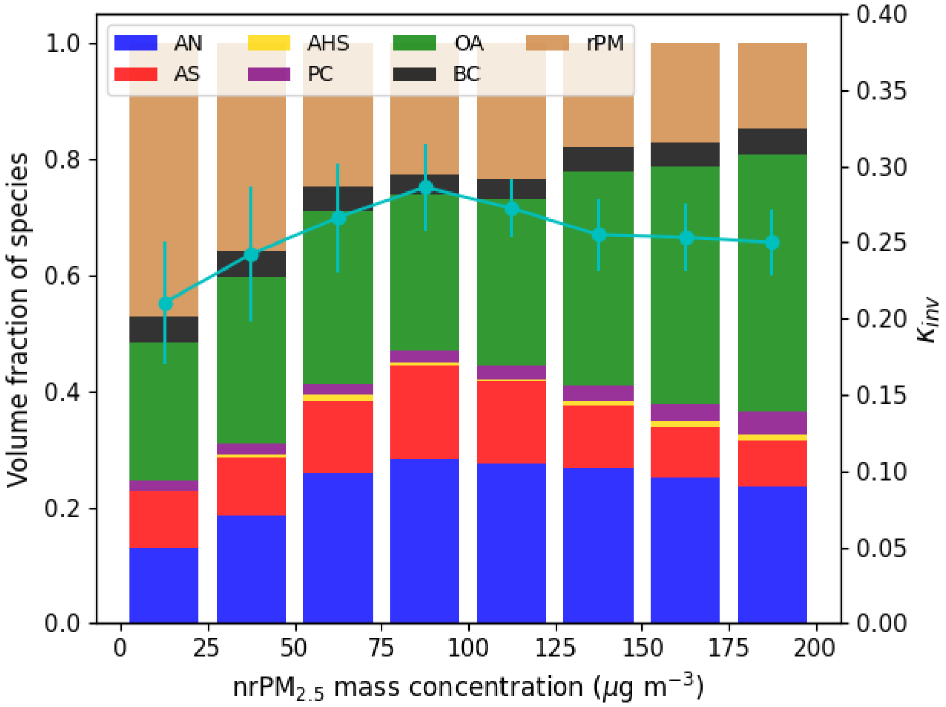

Figure S14: Variations of κ_{inv} and volume fractions of different aerosol species as a function of nrPM$_{2.5}$ mass concentration during the winter campaign

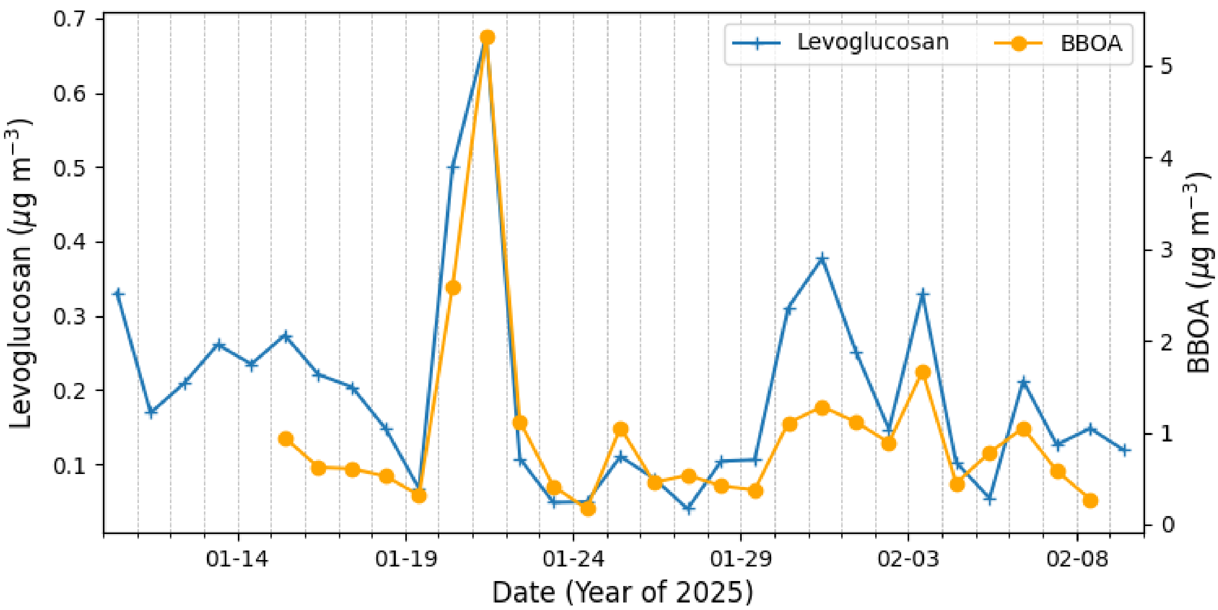

Figure S15: Time series of filter-based levoglucosan mass concentration, a tracer of biomass burning, and the BBOA factor resolved from PMF analysis of ToF-ACSM OA measurements.

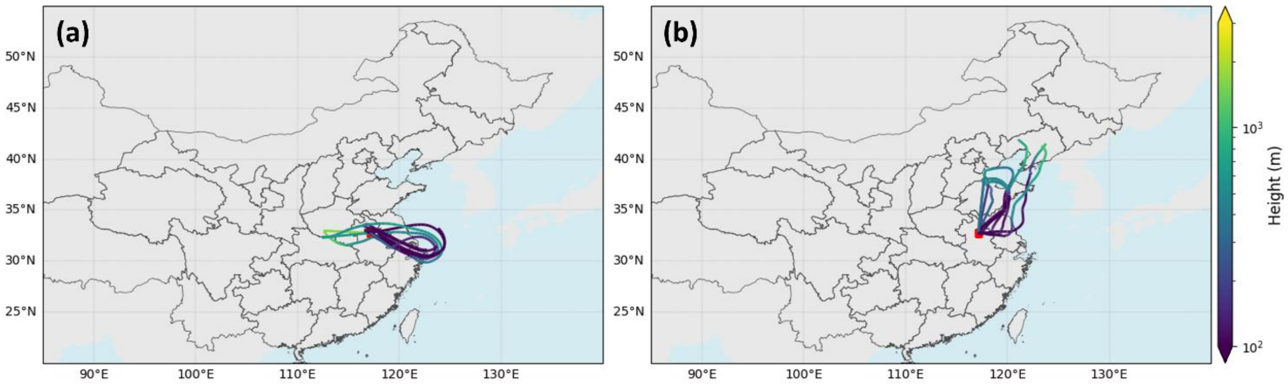

Figure S16: 72-hour backward trajectories arrived at 100 m heigh above the Huainan site during the (a) first stage and (b) second stage of the pollution episode of January 20-25, 2021. The backward trajectories were computed using the NOAA HYSPLIT model, driven by meteorological data from the NCEP Global Data Assimilation System (GDAS) at a spatial resolution of 1°. The HYSPLIT model, which is publicly accessible at https://www.arl.noaa.gov/hysplit/, was employed to generate the trajectories. These trajectories were subsequently overlaid onto the map using a custom Python script.

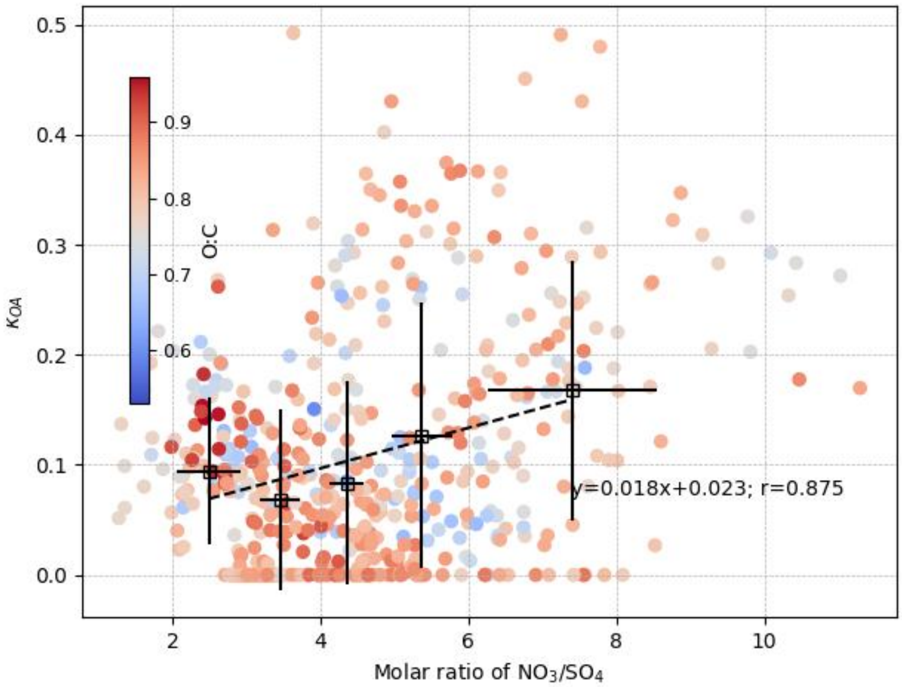

Figure S17: Variation of κ_{OA} as a function of molar ratio of NO_3 to SO_4, with colors indicating the corresponding O:C ratios. Black open squares represent binned mean κ_{OA} values based on NO_3/SO_4 ratio bins defined by 20% percentiles, with error bars indicating one standard deviation. The dashed line shows a linear regression fitted to the binned means.

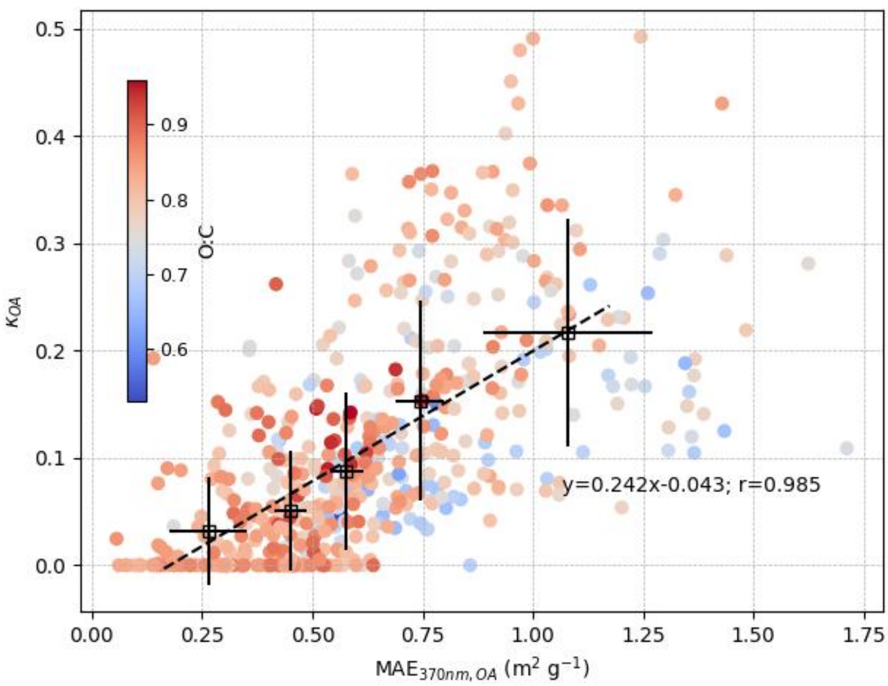

Figure S18: Variation of κ_{OA} as a function of $MAE_{OA,370nm}$, with colors indicating the corresponding O:C ratios. Black open squares represent binned mean κ_{OA} values based on $MAE_{OA,370nm}$ bins defined by 20% percentiles, with error bars indicating one standard deviation. The dashed line shows a linear regression fitted to the binned means.